J Therm Spray Tech
https://doi.org/10.1007/s11666-024-01901-5

ORIGINAL RESEARCH ARTICLE

Novel FeNiCrMoCBPNb High-Entropy Amorphous Coatings Prepared by Atmospheric Plasma Spraying with Excellent Corrosion and Wear Properties

Zhijun Guo[1] · Yangzi Ye[1] · Zhenjie Zhou[1] · Qianqian Wang[1,2] · Baosen Zhang[2] · Baolong Shen[1]

Submitted: 29 May 2024 / in revised form: 6 November 2024 / Accepted: 27 November 2024

Abstract Designing and fabricating Fe-based amorphous coatings with excellent wear and corrosion resistance as surface protection materials are essential to improve the service life of marine equipment. In this work, by adding 1 at.% Nb, a novel $Fe_{34}Ni_{20}Cr_{20}Mo_5B_4C_4P_{12}Nb_1$ high-entropy amorphous alloy with enhanced glass-forming ability and excellent corrosion resistance was designed. The $Fe_{34}Ni_{20}Cr_{20}Mo_5B_4C_4P_{12}Nb_1$ composition was adopted to prepare gas-atomized powders, which were then used as feedstock to prepare coatings using atmospheric plasma spraying (APS) technology with different input power. Higher spraying power was found to lead to denser coating, but more formation of oxides and lower amorphous content. The coating-35 kW input power exhibited the best corrosion resistance in 3.5 wt.% NaCl solution and high hardness of 519 ± 21 HV. The dry sliding wear rate of the coating-35 kW at 20 N and 20 mm/s was 8.3×10^{-7} mm^3/(N m), and the friction coefficient of the coating was 0.17 and kept relatively steady throughout the sliding test. This work guided designing Fe-based high-entropy amorphous coatings from both the composition aspect and the coating preparation technology.

✉ Qianqian Wang
qwang678@seu.edu.cn

✉ Baosen Zhang
baosenzhang@njit.edu.cn

[1] School of Materials Science and Engineering, Jiangsu Key Laboratory for Advanced Metallic Materials, Southeast University, Nanjing 211189, China

[2] School of Materials Science and Engineering, Jiangsu Key Laboratory of Advanced Structural Materials and Application Technology, Nanjing Institute of Technology, Nanjing 211167, China

Keywords atmospheric plasma spraying (APS) · corrosion resistance · Fe-based high-entropy amorphous coatings · wear resistance

Introduction

With the continuous development of marine resources, many marine equipment and facilities have been developed. However, the severe maritime environment, such as dissolved oxygen, hydrostatic pressure, and chloride electrolyte, caused corrosion problems for metallic equipment, resulting in significant economic loss (Ref 1, 2). It was reported that the corrosion problems cost the world about 2.5 trillion USD, estimated to be 3.4% of the global GDP (Ref 3). The Fe-based amorphous alloy coatings with superior corrosion and wear properties, as well as low material cost, are promising surface protection for metallic substrates in various aggressive environments, including erosion–corrosion marine environments, boilers, gas turbines, nuclear industry, etc. (Ref 4). The commonly used amorphous coating preparation methods include flame spraying, arc spraying, atmospheric plasma spraying, high-velocity oxy-fuel spraying, laser cladding, and detonation gun spraying (Ref 5). Among these, atmospheric plasma spraying (APS) is a simple and efficient method for synthesizing high-quality Fe-based amorphous alloy coatings that have a dense structure and strong binding affinity with the substrate (Ref 6).

The Fe-Cr-based amorphous alloys have attracted much attention owing to their excellent corrosion and wear resistance, as well as low material cost. However, their industrial application as a structural material is restricted by the limited glass-forming ability (GFA) and brittleness. Synthesis of Fe-Cr-based amorphous coating via thermal

Published online: 16 December 2024

spraying techniques is considered to be an effective way to overcome this limitation. During the past decades, a series of Fe-Cr-based amorphous alloy coatings have been developed, including FeCrMoPC (Ref 7, 8), FeCrMoBC-SiAl (Ref 9), FeCrMoBCY (Ref 7, 10-12), FeCrMn-MoWBCSi (Ref 13-17), etc. In particular, the SAM1651 ($Fe_{48}Cr_{15}Mo_{14}C_{15}B_6Y_2$) (Ref 18) and SAM2X5 ($Fe_{49.7}$-$Cr_{18}Mn_{1.9}Mo_{7.4}W_{1.6}B_{15.2}C_{3.8}Si_{2.4}$) (Ref 19-21) developed by the US navy exhibit excellent corrosion resistance and have been commercially used. However, these two coatings contained a large content of Mo ($\sim$ 6-16 wt.%) as well as rare earth elements, which increased the cost and limited the industrial applications. Therefore, the synthesis of high-performance Fe-based amorphous alloys using low-cost elements (e.g., B, C, Si, and P) and reducing the use of precious metal elements (e.g., Mo, W, Y) is of great significance for industrial applications. High-entropy alloys (HEAs) have drawn research attention due to their outstanding mechanical properties, including high strength and large ductility, and excellent chemical properties, such as good corrosion resistance (Ref 22). The "high entropy" strategy has been introduced to design amorphous alloys, and a series of high-entropy amorphous alloys have been prepared, such as FeCrNiMoPCB (Ref 23), CoCrBFeNiSi (Ref 24) and FeCoNiCrBSi (Ref 25). Due the synergy between the high-entropy effect and amorphous structure, these alloys exhibited good corrosion and wear performance, making them potential materials for surface protection coatings. Furthermore, Shu (Ref 24) and Cheng (Ref 25) et al. prepared high-entropy amorphous coatings by laser cladding, showing excellent corrosion and wear resistance. However, there is still no report on the preparation of Fe-based high-entropy amorphous coatings using the APS method.

Recently, utilizing the high-entropy designing strategy, the $Fe_{20\text{-}35}Cr_{20\text{-}30}Ni_{20}Mo_{5\text{-}15}(P_{0.6}C_{0.2}B_{0.2})_{20}$ amorphous alloys with excellent thermal stability, strength, and corrosion resistance have been developed (Ref 23). Among these alloys, the $Fe_{35}Ni_{20}Cr_{20}Mo_5B_4C_4P_{12}$ alloy exhibited the best combination of the GFA and corrosion resistance, making it promising for applications as coating materials in aggressive environments. Besides, it has been proved that Nb has positive effects in enhancing the GFA and corrosion resistance of Fe-Cr-based amorphous alloys (Ref 26). Thus, in this work, we studied the effect of minor Nb addition on the GFA and corrosion resistance of Fe_{35}-$Ni_{20}Cr_{20}Mo_5B_4C_4P_{12}$ amorphous alloy. As several kilograms of powders are needed for preparing an APS coating sample, while only several grams of the ingot are needed for preparing a melt-spun ribbon sample, due to the economic benefit, melt-spun ribbon samples were used for the broad composition study in this work. Besides, rod samples were prepared to investigate the GFA of different compositions. Based on the analyses of the ribbon and rod samples, the $Fe_{34}Ni_{20}Cr_{20}Mo_5B_4C_4P_{12}Nb_1$ (at.%) high-entropy amorphous alloy with high GFA, excellent corrosion resistance, and high hardness was obtained and used as the prototype alloy composition for powders and coatings preparation. Then, powders with this composition were prepared using the gas atomization method and used as the feedstock for thermal spray. The coatings were prepared using the APS method with different input power. The relationships between process, microstructure, corrosion resistance, and wear resistance of the coating were systematically investigated. This work demonstrates the great application potential of thermal sprayed Fe-based high-entropy amorphous coatings.

Experimental

Materials and Sample Preparation

Ingots of the $Fe_{35-x}Ni_{20}Cr_{20}Mo_5B_4C_4P_{12}Nb_x$ (x = 0, 1, 3, 5 at.%) alloys were prepared by induction melting mixtures of Fe, Ni, Cr, Mo, Nb, Cr_3C_2, FeB and FeP with purities over 99.5 mass% under argon atmosphere. The ribbons with a cross section of 0.03 mm $\times$ 1.2 mm were prepared by the melt-spinning method. The SAM1651 ribbons were also prepared using the same method for comparison. Cylindrical rods with a length of 40 mm and diameters of 1-2 mm were prepared by copper mold casting. The Fe_{34}-$Ni_{20}Cr_{20}Mo_5B_4C_4P_{12}Nb_1$ (at.%) amorphous powders were synthesized by the gas atomization method. The ingots prepared by induction melting were used as the master alloy for gas atomization. The furnace was vacuumed to 5×10^{-3} Pa. The ingots were melted in the quartz crucible with high-purity argon protection and injected into the chamber. The injected melt was then atomized and cooled by high-pressure argon, and the pressure was kept at 7, 8, and 9 MPa for different samples. Powders with diameters of 25-53 μm were sieved out as feedstock powders for thermal spraying. The 45 steel with a dimension of 100 mm $\times$ 100 mm $\times$ 5 mm was selected as the substrate. Before thermal spraying, all substrates were sand-blasted and ultrasonically cleaned in ethyl alcohol. The amorphous coatings were fabricated by APS thermal spray system (Sulzer Metco 9MC, Sulzer Metco Ltd., China). The detailed spraying parameters are given in Table 1.

Microstructure Characterization

The phase identification of the rods, ribbon, feedstock powder, and coatings was carried out using an x-ray diffractometer (XRD) (Bruker D8 Advance; Cu-Kα radiation). The nanostructure of samples was investigated by

Table 1 Spraying parameters employed in the APS process

Parameters	Values
Primary plasma gas flow rate (Ar, L min^{-1})	75
Auxiliary plasma gas flow rate (H_2, L min^{-1})	7.3
Moving speed (mm/s)	1000
Powder feed rate (g min^{-1})	25
Spray distance (mm)	120
Spray power (kW)	28, 35, 42

transmission electron microscopy (TEM) (Talos F200X, Thermo Fisher Scientific). The thermal properties of the samples were analyzed by differential scanning calorimetry (DSC) (404F3, Netzsch), and the heating rate was 0.67 K/s. The morphology and composition of the powders and coatings were characterized by scanning electron microscopy (SEM) (Sirion 200, FEI) coupled with an energy dispersive spectrometer (EDS). The porosity of the coatings was counted from the cross-section SEM images (magnification 500x) by ImageJ software (k 1.45), and the given porosity value was averaged from 10 counting results. The composition of powders was also analyzed by electron probe x-ray micro-analyzer (EPMA) (JXA-iHP200F).

Electrochemical Measurements

Electrochemical measurements were conducted using the electrochemical workstation (Gamry interface 1000) in 3.5 wt.% NaCl, 0.5 M H_2SO_4, and 1.0 M HCl solution open to air at room temperature. 3.5 wt.% NaCl is a simulation of seawater. 0.5 M H_2SO_4 and 1.0 M HCl solution were chosen to investigate the corrosion behavior of the alloys in an acidic environment by keeping the H^+ concentration to 1.0 M. Besides, 1.0 M HCl solution provides the synergistic effect of H^+ and Cl^-. The samples, platinum, and Ag/AgCl electrodes corresponded to the working, counter, and reference electrodes, respectively. Before the electrochemical tests, the coating samples (1 cm × 1 cm × 0.5 cm) were embedded in epoxy resin and then polished to a mirror finish with an exposed area of 1 cm^2. Potentiodynamic polarization measurements were performed from − 0.5 to 1.5 V at a potential scanning rate of 0.5 mV/s. Before potentiodynamic polarization measurement, the samples were open-circuit immersed for about 30 min until the open-circuit potentials became almost steady. For comparison, the potentiodynamic polarization measurements of 45 steel and SAM1651b amorphous ribbon were also conducted in the same way. EIS measurements were performed at frequencies from 10^5 to 10^{-2} Hz with a sinusoidal amplitude of 10 mV. The EIS data were fitted using the Z_{view} software.

Salt spray tests were conducted according to GB6458-86. All the coating samples (1 cm × 1 cm × 0.5 cm) were sealed with silicone and cleaned with acetone before exposure to salt fog. The salt spray tests accord with the following conditions: The sprayed solution was 5 wt.% NaCl solution with a pH between 6.5-7.2 and the coated samples, with the protected face upwards, suspended in a salt spray test chamber (YWX/Q-250, China). The tests were performed with a working temperature of 35 ± 2 °C and settlement of 1-2 ml/80 cm^2/h for a total exposure time of 200 h. Photographs were taken before and after exposure every 20 h to document the surface conditions.

Mechanical Measurements

The Vickers hardness (HV) was measured with a Vickers hardness tester (FM-700) under 300 gf (2.94 N) for 10 s. The sliding wear tests were carried out on a reciprocating ball-on-block tribometer (Rtec MFT-5000) using a silicon nitride ball (manufacturer's nominal hardness 2200 HV; diameter = 12.7 mm) as the counterpart. Before the wear test, all of the samples were polished to a mirror finish. The parameters for the wear test are listed as follows: reciprocating distance of 2 mm, applied load of 20 and 30 N, sliding speed of 20 and 30 mm s^{-1}, and sliding time of 20 min. The wear rate was calculated by the equation $Q = V/FS$, where Q is the specific wear rate (mm^3 N^{-1} m^{-1}), V is the wear volume (mm^3), F is the applied load (N), and S is the sliding distance (m), respectively. The wear volume (wt. of wear loss/density of coating) was measured from the weight loss of the samples after performing the wear test. The wear properties of 45 steel were also measured using the tribological tests in the same way.

Results and Discussion

Effect of Nb Addition on Properties of Alloy

Figure 1(a) shows the XRD patterns of the $Fe_{35-x}Ni_{20}Cr_{20}Mo_5Nb_xB_4C_4P_{12}$ (x = 0, 1, 3, 5 at.%) ribbons. For all the ribbons, the XRD pattern only shows one broad diffusive peak for each sample, which was characteristic of an amorphous structure. Figure 1(b) presents the DSC curves of the ribbons, and three exothermic peaks caused by the crystallization of different phases were observed in all the DSC curves. Glass transition, which was an endothermic phenomenon before crystallization, was also observed, and the onset temperature of the glass transition process was defined as the glass transition temperature (Ref 27). The glass transition temperature T_g, crystallization

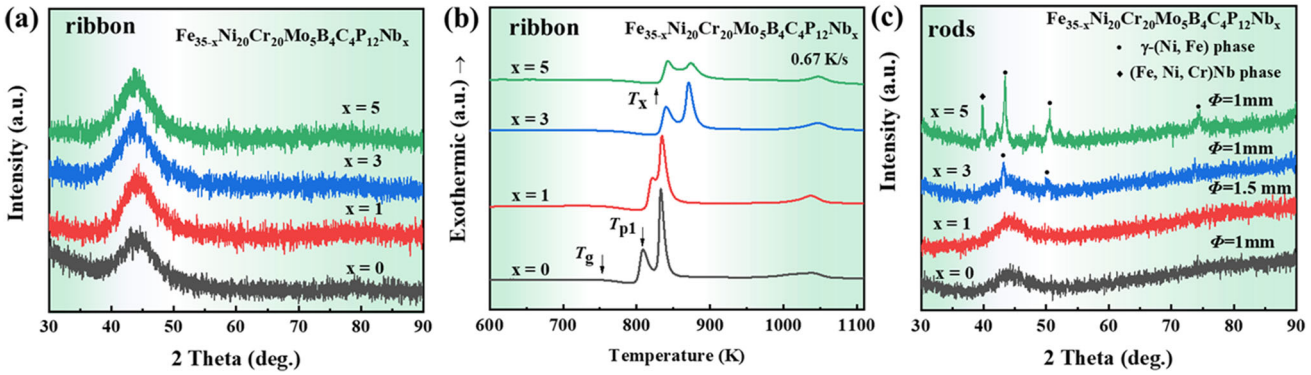

Fig. 1 (a) XRD patterns and (b) DSC curves of as-cast $Fe_{35-x}Ni_{20}Cr_{20}Mo_5B_4C_4P_{12}Nb_x$ (x = 0, 1, 3, 5) ribbons, (c) XRD patterns of as-cast $Fe_{35-x}Ni_{20}Cr_{20}Mo_5B_4C_4P_{12}Nb_x$ (x = 0, 1, 3, 5) rods with diameters of 1-1.5 mm

temperature T_{x1}, and the first crystallization peak temperature T_{p1} were marked with arrows, and the corresponding data are summarized in Table 2. With the increase in Nb content, the T_g increased from 754 to 772 K, and T_{x1} increased from 798 to 830 K, which indicated that the addition of Nb can improve the thermal stability of the alloy. When x = 1, the first and second crystallization peaks of the alloy tended to coincide; with further increasing Nb content, the crystallization peaks separated again. When the crystallization peaks tended to overlap with each other, the composition was approaching the eutectic point, and crystallization at the two exothermic temperatures competed with each other, thus the crystallization process is inhibited (Ref 26, 28). It has been proved that partial replacement of Fe with Nb can effectively improve the GFA due to the greater negative mixing enthalpy between Nb and the metalloid elements (Ref 29, 30). As the melting temperature of niobium is much higher than that of iron, replacing iron with niobium raised the characteristic temperatures of the alloys to higher temperatures. Figure 1(c) shows the XRD patterns of as-cast $Fe_{35-x}Ni_{20}Cr_{20}Mo_5B_4C_4P_{12}Nb_x$ (x = 0, 1, 3, 5) rods with diameters of 1-1.5 mm. Among them, when x = 0 and x = 1, the rod showed a diffuse diffraction peak with no detectable sharp diffraction peak, indicating a completely amorphous structure. However, sharp diffraction peaks from crystallites corresponding to γ-(Fe, Ni) phase were observed in the x = 3 alloy, accompanied by the (Fe, Ni, Cr)Nb phase observed in the x = 5 alloy. These results revealed that a minor addition of Nb (x = 1) improved the GFA of the alloy, while excessive addition jeopardized the GFA. Furthermore, the mixing entropy of $Fe_{34}Ni_{20}Cr_{20}Mo_5B_4C_4P_{12}Nb_1$ is represented by its configurational entropy, and calculated to be 1.72 R using the following equation (Ref 31):

$$\Delta S_{conf} = -R\sum_{i=1}^{n} x_i \ln x_i$$

Table 2 Thermal properties of $Fe_{35-x}Ni_{20}Cr_{20}Mo_5B_4C_4P_{12}Nb_x$ (x = 0, 1, 3, 5) alloys

Alloys	T_g, K	T_{x1}, K	$\triangle T$, K	T_{p1}, K
x = 0	754	798	44	808
x = 1	753	812	59	821
x = 3	768	830	62	840
x = 5	772	830	58	843

where x_i is the mole fraction of the i-th element, and R is the molar constant of ideal gas. Thus, the $Fe_{34}Ni_{20}Cr_{20}Mo_5B_4C_4P_{12}Nb_1$ is a high-entropy amorphous alloy.

To investigate the corrosion behavior of the $Fe_{35-x}Ni_{20}Cr_{20}Mo_5B_4C_4P_{12}Nb_x$ (x = 0, 1, 3, 5) alloys, the potentiodynamic polarization measurements were carried out in 3.5 wt.% NaCl solution at 298 K open to the air, as shown in Fig. 2(a), with the corrosion potential (E_{corr}) and corrosion current density (I_{corr}) summarized in Table 3. By adding 1 at.% Nb, the corrosion potential of the alloy increased from − 229 to − 113 mV, and the corrosion current density decreased from 6×10^{-7} to 5×10^{-7} A/cm^2. As the content of Nb increased to 3 and 5 at.%, the corrosion potential of the alloy decreased slightly, and the current transient peak appeared in the polarization curve, which may be related to the metastable pitting corrosion on the sample surface. The deterioration of corrosion resistance with the increase in Nb content may be attributed to the precipitated nanocrystalline phases, which promoted the initiation of pitting corrosion. Furthermore, the corrosion behavior of $Fe_{34}Ni_{20}Cr_{20}Mo_5B_4C_4P_{12}Nb_1$ ribbon was compared with SAM1651 amorphous ribbon and 304 SS in saline, acidic, and alkaline solutions, and the E_{corr} and I_{corr} are also summarized in Table 3. In 3.5 wt.% NaCl solution (Fig. 2b), the $Fe_{34}Ni_{20}Cr_{20}Mo_5B_4C_4P_{12}Nb_1$ metallic glass spontaneously passivated without pitting when potential < 1.1 V, whereas SAM

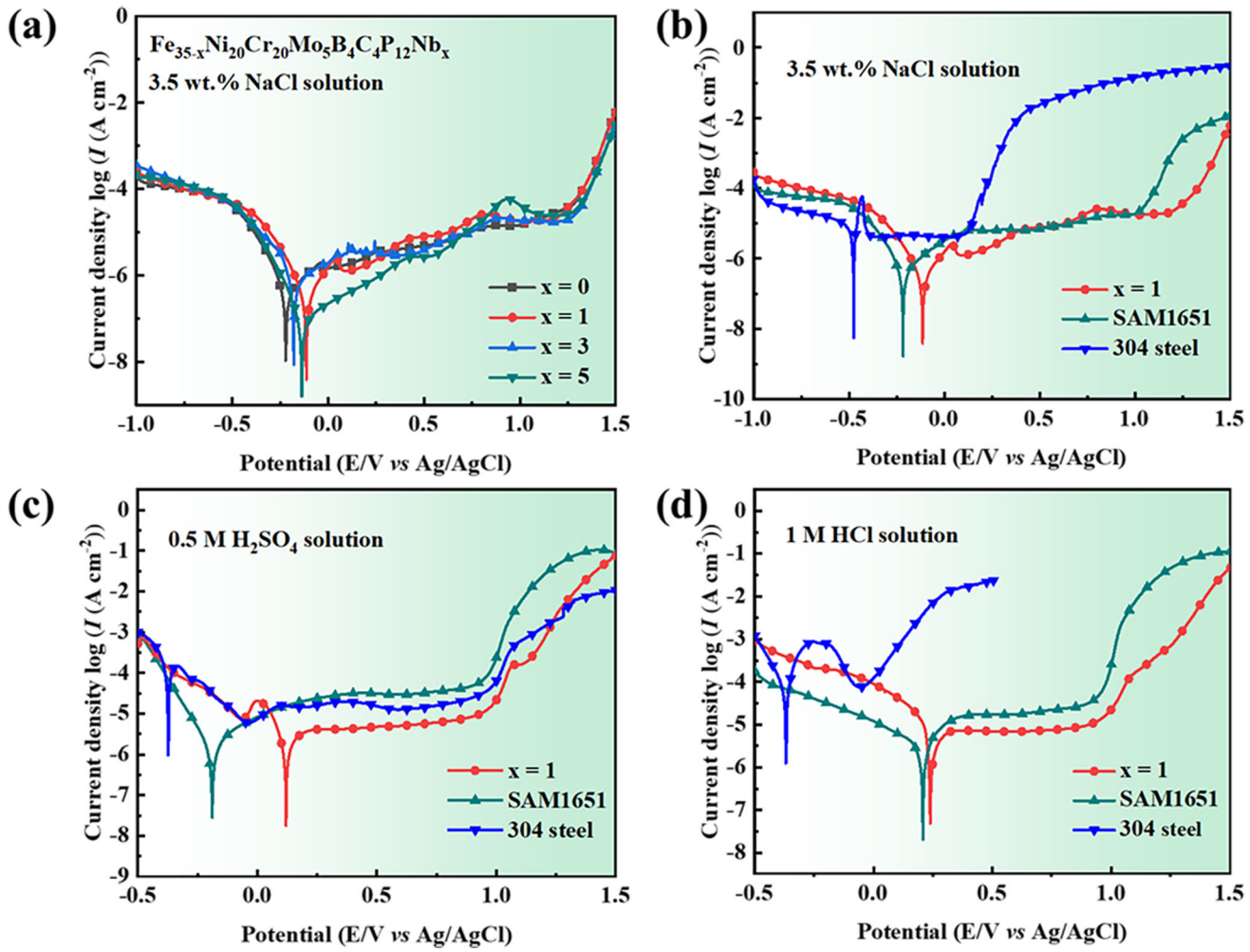

Fig. 2 (a) Potentiodynamic polarization cues of $Fe_{35-x}Ni_{20}Cr_{20}Mo_5B_4C_4P_{12}Nb_x$ (x = 0, 1, 3, 5) in 3.5 wt.% NaCl solution, (b–d) potentiodynamic polarization curves of $Fe_{34}Ni_{20}Cr_{20}Mo_5B_4C_4P_{12}Nb_1$, SAM1651 ribbons and 304 stainless steel in 3.5 wt.% NaCl, 0.5 M H_2SO_4 and 1 M HCl solution

Table 3 Electrochemical parameters of $Fe_{35-x}Ni_{20}Cr_{20}Mo_5Nb_xB_4C_4P_{12}$ (x = 0, 1, 3, 5), SAM1651 alloys and 304 SS

Alloys	3.5 wt.% NaCl		0.5 M H_2SO_4		1 M HCl	
	E_{corr}, mV	I_{corr}, A/cm^2	E_{corr}, mV	I_{corr}, A/cm^2	E_{corr}, mV	I_{corr}, A/cm^2
x = 0	− 229	6×10^{-7}	…	…	…	…
x = 1	− 113	5×10^{-7}	119	4.6×10^{-6}	293	1.4×10^{-5}
x = 3	− 179	7×10^{-7}	…	…	…	…
x = 5	− 140	7×10^{-8}	…	…	…	…
SAM1651	− 240	6×10^{-7}	− 189	3.1×10^{-6}	207	1.2×10^{-5}
304 SS	− 490	6×10^{-6}	− 385	8×10^{-5}	− 368	1.7×10^{-4}

1651 and 304 get pitted at 1 V and 0.1 V respectively, as suggested from the sharp rise of the current density. In addition, the E_{corr} of $Fe_{34}Ni_{20}Cr_{20}Mo_5B_4C_4P_{12}Nb_1$ was higher than SAM1651 and 304 SS, indicating its superior corrosion resistance to the Cl^-. In 0.5 M H_2SO_4 solution (Fig. 2c), all of the samples exhibited pronounced spontaneous passivation followed by a large passive region until the potential reached 1.0 V. The $Fe_{34}Ni_{20}Cr_{20}Mo_5B_4C_4P_{12}Nb_1$ alloy possessed the noblest E_{corr} of 119 mV, and the lowest I_{corr} of 4.6×10^{-6} A/cm^2, indicating its outstanding corrosion resistance to H^+. In 1 M HCl solution (Fig. 2d), the 304 SS got pitted at low potential, whereas $Fe_{34}Ni_{20}Cr_{20}Mo_5B_4C_4P_{12}Nb_1$ alloy and SAM1651 showed spontaneous passivation without pitting with potential < 1.0 V. The E_{corr} of

$Fe_{34}Ni_{20}Cr_{20}Mo_5B_4C_4P_{12}Nb_1$ alloy was nobler and I_{corr} was lower than SAM1651, revealing $Fe_{34}Ni_{20}Cr_{20}Mo_5B_4C_4P_{12}Nb_1$ alloy's excellent corrosion resistance to the combined H^+ and Cl^- than that of 304 and SAM1651. Previous research indicated that the formation of a dense Nb_2O_5 film on the surface of Fe-based amorphous alloy with Nb addition could enhance the pitting resistance (Ref 30, 32, 33), which may explain the excellent corrosion resistance of $Fe_{34}Ni_{20}Cr_{20}Mo_5B_4C_4P_{12}Nb_1$ amorphous alloy.

Microstructure of Powders and Coatings

Since the $Fe_{34}Ni_{20}Cr_{20}Mo_5B_4C_4P_{12}Nb_1$ amorphous alloy exhibited the largest GFA and best corrosion resistance, the powders with this composition were prepared using gas atomization with different atomization pressures. The composition of amorphous powder was measured by EDS and EPMA with the results shown in Table 4, which was quite close to the nominal composition. The morphology of the $Fe_{34}Ni_{20}Cr_{20}Mo_5B_4C_4P_{12}Nb_1$ powders produced at varying atomization pressures are shown in Fig. 3(a), (b), and (c). It can be seen that the majority of particles produced under 7 MPa were spherical or near-spherical with diameters of 50-75 μm. The powders prepared under 8 MPa exhibited good sphericity with diameters of 40-50 μm along with small satellites. When the atomization pressure reached 9 MPa, spherical powders (diameter: 30-50 μm) with few satellites were observed. The absence of satellites and good sphericity usually leads to good fluidity during thermal spraying (Ref 34). Figure 3(d) presents the XRD patterns of the powders with different atomization power. A small sharp peak appeared on the broad diffuse halo at approximately 45° diffraction angle (2θ) under 7 MPa, indicating that the powder was mostly amorphous with a small amount of crystalline content ($Fe_{23}B_6$). The powders prepared under 8 and 9 MPa showed almost fully amorphous structure within the resolution limit of XRD. The DSC curves of the powders processed at atomization pressure of 7, 8, and 9 MPa are shown in Fig. 3(e). The amorphous contents of the powders were calculated by comparing the enthalpy of crystallization derived from the DSC curves with that of the $Fe_{34}Ni_{20}Cr_{20}Mo_5B_4C_4P_{12}Nb_1$ ribbon sample (Fig. 1b) (Ref 27, 35). The amorphous contents of the powders processed at atomization pressure of 7, 8, and 9 MPa were 75, 80, and 86%, respectively. This result indicated that the automerization pressure could affect the formation of the amorphous phase. The lowest amorphous content of the powders prepared under 7 MPa may result from its larger particle size. As the powders prepared under 9 MPa have both better sphericity and larger amorphous content, they are more appropriate to be used to prepare thermal spraying coatings.

Table 4 Chemical composition of FeNiCrMoBCPNb alloy powder obtained from EDS and EMPA analyses (at.%)

Elements	Fe	Ni	Cr	Mo	Nb	B	C	P
EDS	35.9	21.9	19.5	5.9	1.8	2.7	2.9	9.4
EPMA	34.5	18.7	19.8	4.6	1.1	…	9.3	12

Figure 3(f) shows the XRD patterns of the coatings prepared by the APS method at different spraying power, i.e., 28, 35, and 42 kW. The appearance of a diffuse peak of the amorphous phase between 40° to 50° indicated all the three coatings had a relatively high amorphous content. When the power was 28 kW, no sharp diffraction peak appeared, indicating the coating was amorphous. As the spraying power increased to 35 and 42 kW, distinct sharp peaks corresponding to Cr_2O_3 appeared (Ref 36). The amorphous content, which was calculated from the enthalpy of crystallization (the DSC data not shown), decreased as the spraying power increased, namely 75% for 28 kW, 72% for 35 kW, and 65% for 42 kW. With higher plasma power, during solidification of the molten splats, the heat might build up and lead to decrease in the solidification rate, and thus promoted crystallization. Besides, excessive heat input resulted in oxidation in smaller powder particles, which prevented them from fusion and spreading. The oxides can serve as nucleation sites for crystallization (Ref 37-39). Thus, the amorphous content decreased with increasing spraying power.

The cross-section morphology of the coatings prepared at different spraying powers is shown in Fig. 4. It was found that all the coatings with a thickness of $\sim$ 250 μm were well-bonded to the substrate. For the coating sprayed under 28 kW, stacks of flat pancake-like molten splats and some incompletely melted spherical and elliptic particles were observed, and the porosity was $\sim$ 5.2% (Fig. 4a, a_1). When the spraying power increased to 35 kW, the coating had a dense structure with reduced porosity (3.25%), but still a small number of unmelted particles and intersplat regions (Fig. 4b, b_1). As the spraying power increased to 42 kW, the coating exhibited a very dense structure with porosity less than 1.75% (Fig. 4c, c_1). In addition, as shown in Fig. 4(c_1), a large amount of dark lamellar structure was observed. An EDS line scan was carried out across one of the lamellar, denoted by the white line in Fig. 4(c_1), and the results are shown in Fig. 4(d). The lamellar was enriched with Cr and O, suggesting it was mainly composed of Cr_2O_3 (Ref 38), which was consistent with the result in Fig. 3(f). These results implied that higher spray power not only provided higher energy to melt the powders to form a denser coating, but also led to oxidation during the spraying process. The hardness of the coatings was

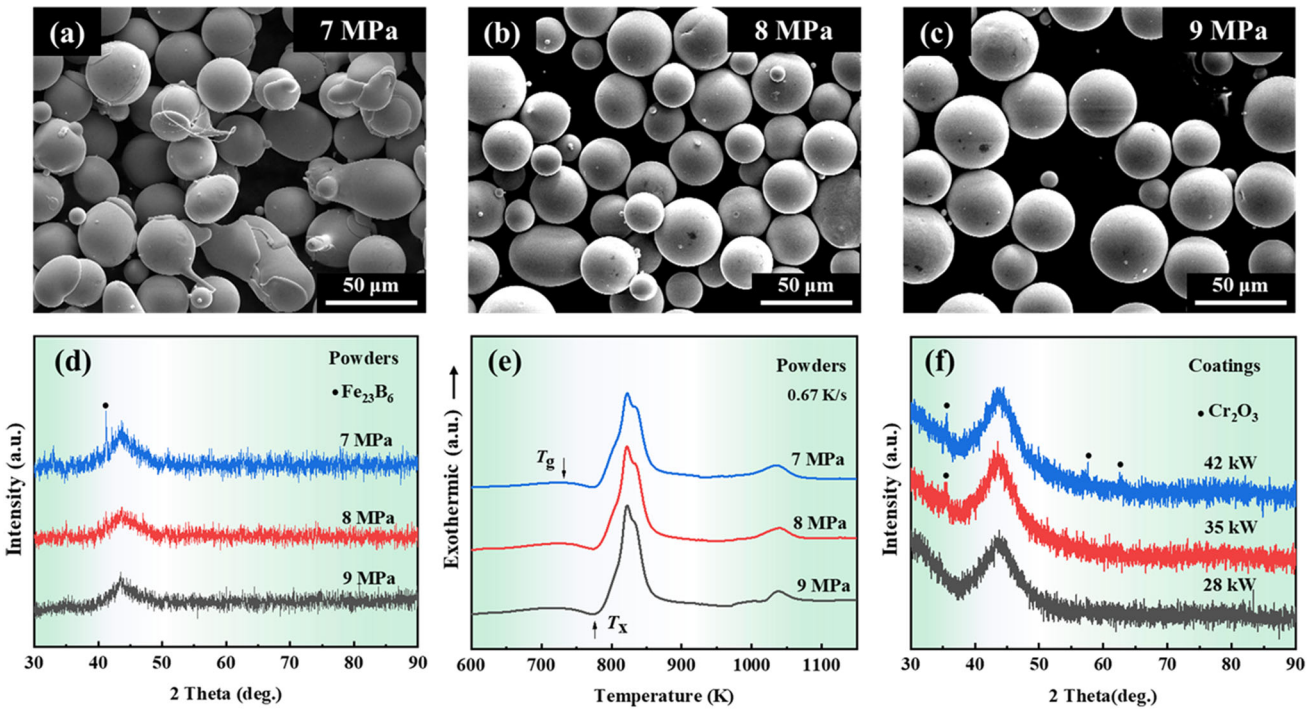

Fig. 3 $Fe_{34}Ni_{20}Cr_{20}Mo_5B_4C_4P_{12}Nb_1$ amorphous powders processed by different atomization pressures: (a–c) SEM images, (d) XRD patterns, (e) DSC curves, (f) XRD patterns of the coatings prepared with different spraying power

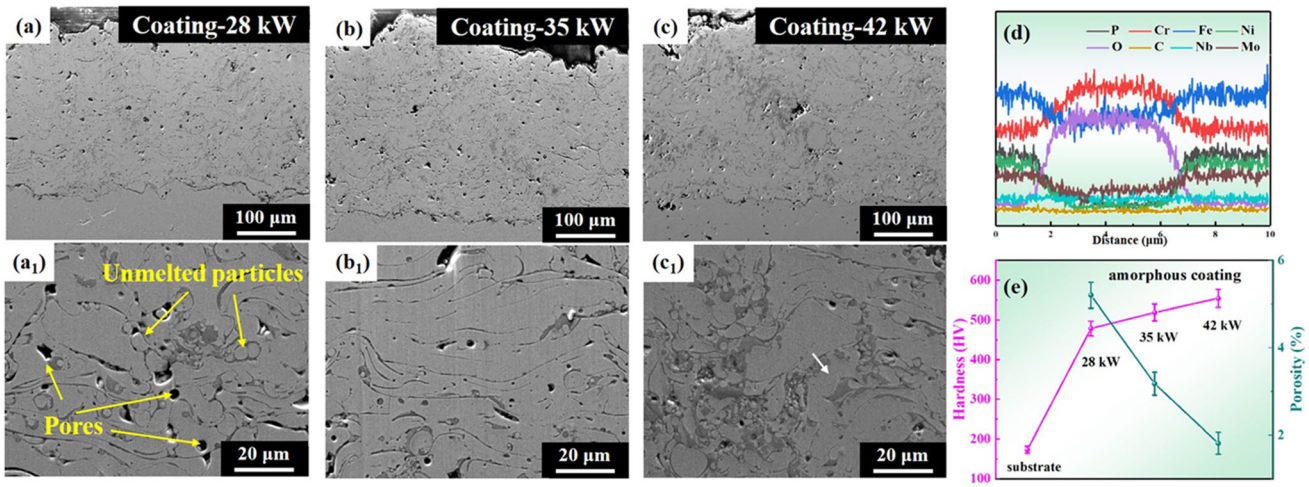

Fig. 4 Cross-section microstructure of Fe-based amorphous coatings prepared with different spraying power (a, a_1) 28 kW, (b, b_1) 35 kW, (c, c_1) 42 kW, (d) EDS line scanning, (e) porosity and hardness

measured, and the results are shown in Fig. 4(e), together with the values of the porosity. The hardness of coating-28 kW, coating-35 kW, and coating-45 kW were 479 ± 19, 519 ± 21 and 554 ± 23 HV, all of which were much higher than the 45 steel substrate (173 ± 9 HV). The coating sprayed at 42 kW showed the highest hardness due to its increased oxide content.

To obtain detailed microstructure information of the matrix and the intersplat regions, TEM observations were carried out on the coating sprayed at 35 kW (Fig. 5a, a_1). Some crystalline phases with dimensions from 5 to 50 nm were distributed in the amorphous matrix. The composition of these nanocrystalline phases was analyzed by EDS, indicating these phases were depleted in Fe, Ni, and rich in Cr, O in comparison with the amorphous matrix. As shown in the HR-TEM image in Fig. 5(a_1), lattice fringes were observed in the particle, indicating the particles are crystallized. Furthermore, Fig. 5(b) shows that the interparticle oxide layers were composed of a large number of grains distributed in the matrix. The selected area electron

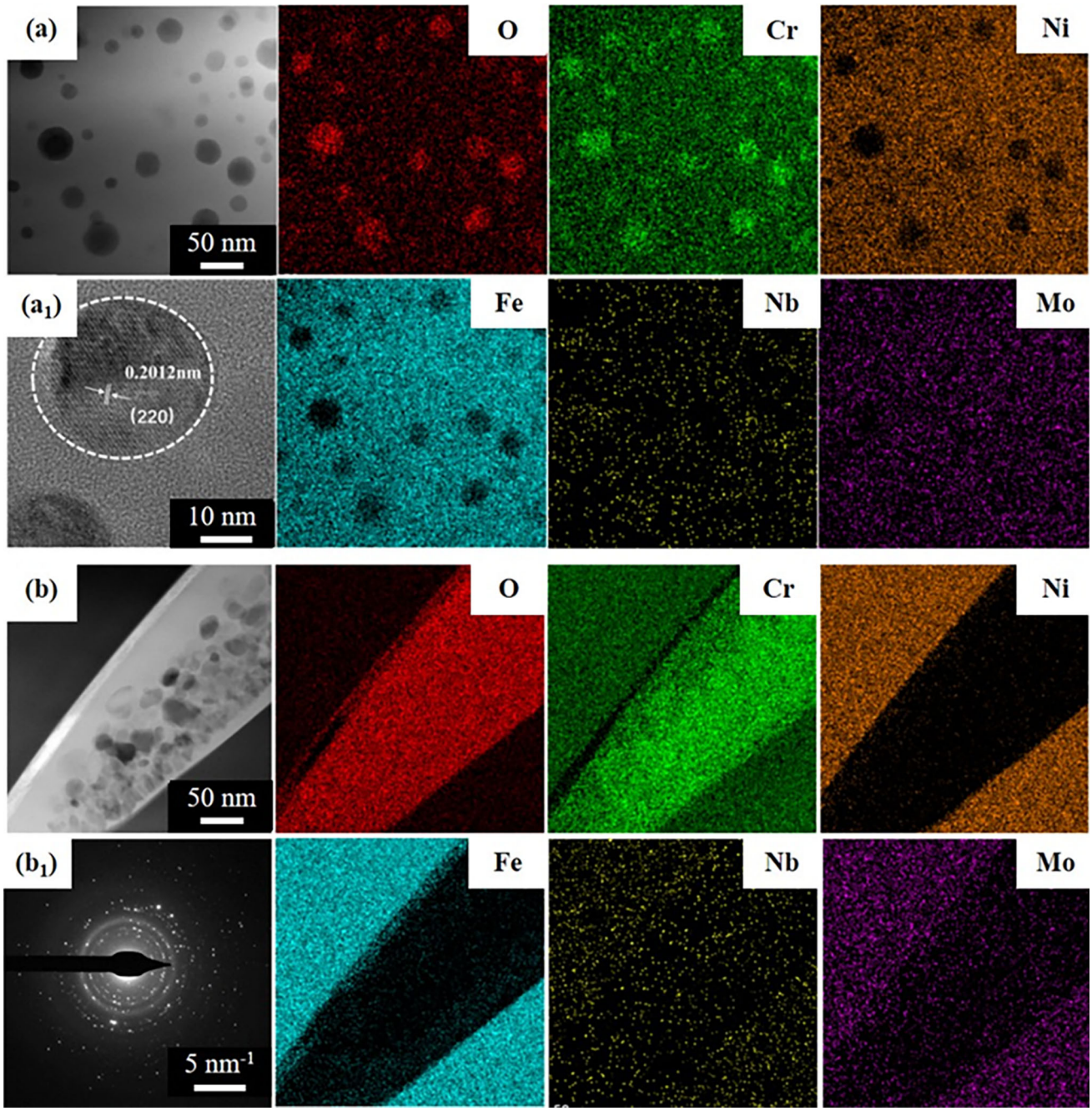

Fig. 5 (a) TEM image and element distribution of precipitates in amorphous coating, (a_1) HR-TEM image of one precipitate, (b) TEM image and element distribution of precipitates in the interparticle region and (b_1) its SAED pattern

diffraction (SAED) patterns in Fig. 5(b1) shows characteristics of multiple crystallites, and the diffraction rings corresponded to the Cr_2O_3 phase. The EDS analysis revealed that crystalline grains were also rich in Cr and O. Besides, the chromium concentration at the interface between the splat region and the matrix was extremely low. This suggested that the formation of Cr_2O_3 results in the Cr-poor area near the splats. The results implied that the interface of the interparticle was highly oxidized during the spraying and led to the formation of (Fe, Cr)-oxides.

Corrosion Behavior of Coatings

The corrosion properties of the Fe-based amorphous coatings were investigated in 3.5 wt.% NaCl solution using the electrochemical tests. The potentiodynamic polarization

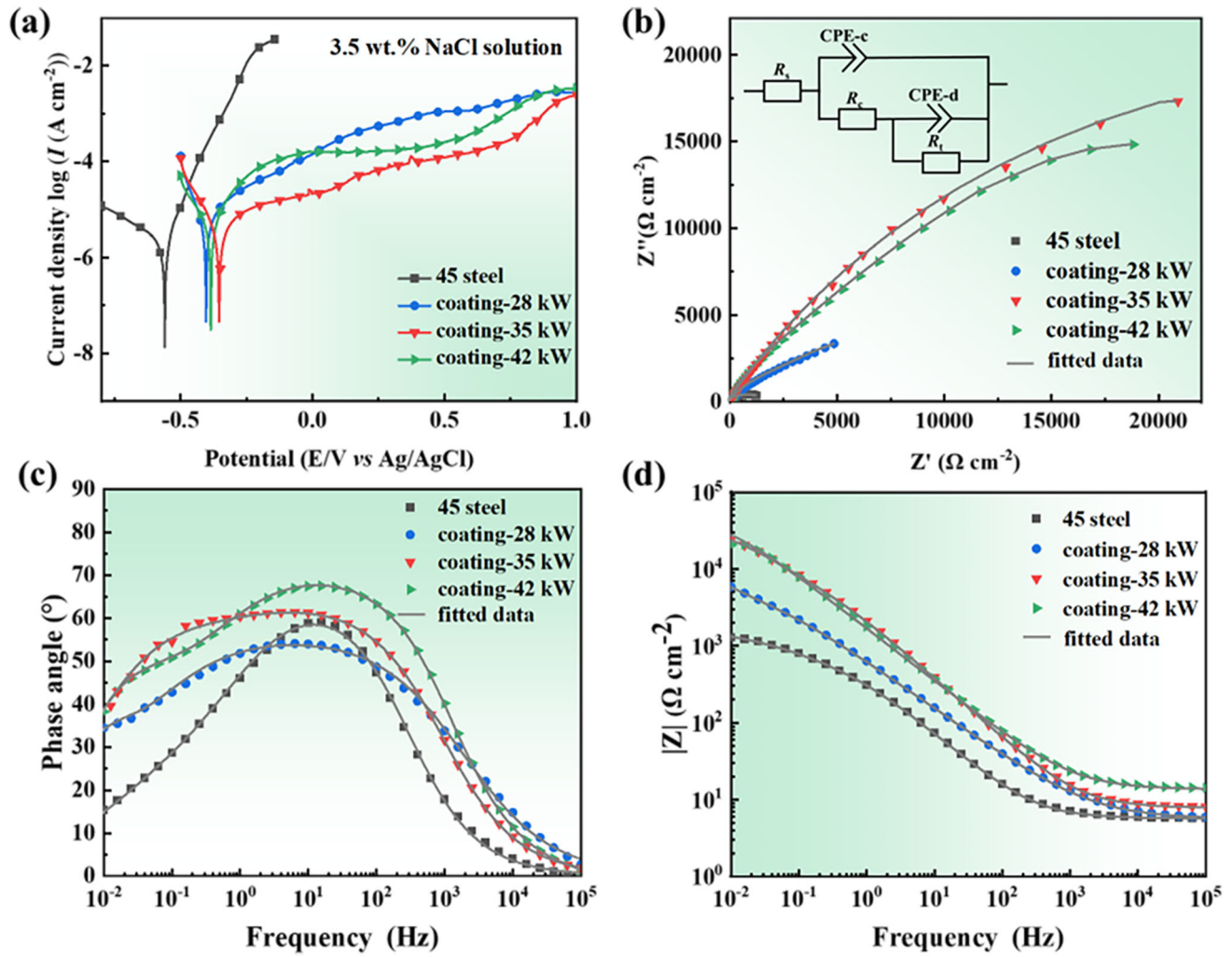

Fig. 6 (a) Polarization curves of amorphous coatings prepared by different spraying power in 3.5 wt.% NaCl solution compared with 304 steel, electrochemical impedance behavior of different coatings samples in 3.5 wt.% NaCl solution (b) Nyquist plots, (c) Bode impedance magnitude plots, (d) Bode phase angle plots

Table 5 Electrochemical parameters of the coatings and 45 steel substrate

Samples	E_{corr}, mV	I_{corr}, A/cm^2	I_{pass}, A/cm^2
Substrate	− 560	2.8×10^{-5}	…
Coating-28 kW	− 428	6.8×10^{-6}	3.9×10^{-4}
Coating-35 kW	− 335	5.1×10^{-6}	3.1×10^{-5}
Coating-42 kW	− 386	5.9×10^{-6}	1.5×10^{-4}

curves of the coatings were measured and compared with 45 steel, as shown in Fig. 6(a), and the corresponding electrochemical values, including E_{corr}, I_{corr}, and passivation current density (I_{pass}), are listed in Table 5. Passivation was observed on the polarization curves of the coatings, but not on that of 45 steel. The I_{corr} values for the three coatings were almost the same, indicating that the intrinsic corrosion rate before the passivation of the coatings was similar. The coating-35 kW showed the highest E_{corr} (−335 mV) and the lowest I_{pass} (3.1×10^{-5} A/cm^2), indicating the better corrosion resistance of the coating-35 kW in the saline environment (Ref 40). Besides, the I_{pass} value of the coating initially increased and then decreased with increasing spraying power. This is due to the two competing processes at elevated power. On the one hand, as the spraying power increased from 28 to 42 kW, a greater amount of powder melted, leading to a decrease in porosity. On the other hand, crystallization was promoted with higher input power causing the galvanic effect. The superior corrosion properties of the coating-35 kW are attributed to a better combination of low porosity and high amorphous content. In Nyquist plots (Fig. 6b), the capacitive diameter of coating-35 kW was higher than coating-

28 kW and coating-42 kW, suggesting that the passive film of coating-35 kW provided a more effective barrier. The equivalent circuit model (EEC) of the amorphous coatings is shown in the inset of Fig. 6(b). For the EEC model, R_s, R_c, and *CPEc* denoted the solution resistance, the coating resistance, and the non-ideal capacitance of the corrosion product film, respectively. The CPEd and R_t represented the double layer capacitance and the charge transfer resistance of corrosion reaction in the defects. Noteworthy, phase angle curves of all coatings showed one shoulder and two-time constants, as displayed in Fig. 6(c). As shown in Fig. 6(c) and (d), the impedance values and phase angle of coating-35 kW and coating-42 kW were higher than those of substrate and coating-28 kW, indicating that pores had a greater influence on the corrosion performance of the coating.

The results of EIS fitting for the coatings and 45 steel are presented in Table 6. As the Chi-square χ^2 was within the range from 2×10^{-4} to 8×10^{-4}, the equivalent circuit was rational, and the fitting results were reliable. All constant *n*-(CPE-*T*) values were < 1, which meant the circuit consisted of constant phase elements, not pure capacitance. The variation of R_s was very small and therefore had a negligible effect on the corrosion process. The impedance values in the low-frequency range in the Bode impedance diagram (Fig. 6b) were related to the R_t during corrosion. A elevated impedance amplitude signified a higher R_t, which correlated with better corrosion resistance of the coating. The R_c and R_t of coating-35 kW were larger and could reach 14,685 and 49,825 $\Omega \cdot cm^2$, respectively, indicating the coating-35 kW had better corrosion resistance.

The salt spray tests of the three coatings were conducted for a total exposure time of 200 h, with 45 steel for comparison (Fig. 7). The 45 steel showed completely severe corrosion with rust covering the surface after only 20 h exposure, revealing the worst salt resistance. In comparison, the Fe-based amorphous coatings did not show any signs of corrosion after 20 h exposure. The coating-28 kW and coating-42 kW lost tarnish after 72 h exposure, whereas coating-35 kW was maintained intact. After 200 h, the coating-28 kW was aggressively attacked, moderate pitting was observed, and slight pitting appeared on the surface of coating-42 kW. However, the coating-35 kW showed an almost intact surface accompanied by edge rust stain, demonstrating good impermeability even after 200 h exposure. As coating-28 kW was most severely corroded, its surface morphology after 200 h salt spray test was analyzed by SEM, with the result shown in Fig. 7(e). A lot of corrosion pits were observed. The pits tend to appear near the gray area, which was the oxidized inclusion. The oxides in the coating were mainly Cr_2O_3, consuming Cr element in the matrix, leading to the formation of a local Cr-poor region. This was the origin of galvanic corrosion, which then developed into a steady state pitting corrosion under chloride ion attack. Based on the above results, the long-term corrosion resistance of the Fe-based amorphous alloy coatings was much more sensitive to the coating defects including pores and oxides. The more porosity defects and crystalline/oxidized phases that the coating contained, the worse the long-term corrosion resistance was.

Wear Resistance of Coating-35 kW

The wear resistance of the coating-35 kW and 45 steel was tested under 20 N with a sliding rate of 20 mm/s with a silicon nitride ball as the counterpart. The average wear volume after sliding tests is shown in Fig. 8(a). The coating-35 kW demonstrated superior wear resistance, with its wear volume being roughly one-tenth of that observed in 45 steel. Figure 8(b) shows the variation of the friction coefficient with the sliding time for coating-35 kW and 45 steel. The friction coefficient of coating-35 kW was close to 0.17, which was much lower than that of 45 steel (0.7), implying that the coating kept slower wear loss for even much longer service time. Despite the lack of tungsten (W) and a minimal amount of molybdenum (Mo), the coating-35 kW showed significant resistance to wear,

Table 6 Values of fitting parameters obtained from EIS spectra

Samples	Coating-28 kW	Coating-35 kW	Coating-42 kW	45 steel
R_s, Ω cm^2	5.73	14.05	8.08	5.79
CPEc- *T*, μF cm^{-2} s^{n-1}	48.46	14.31	18.16	58.36
CPEc-n	0.63	0.71	0.78	0.76
R_c, Ω cm^2	7600	14685	13760	577
CPEd-*T*, μF cm^{-2} s^{n-1}	237.6	3.57	14.43	188.4
CPEd-n	0.91	0.61	0.69	0.49
R_t, Ω cm^2	5909	49825	43290	1293
R ($R = R_c + R_t$ Ω cm^2)	13509	64510	57050	1870
χ^2 (10^{-4})	2.9	2.5	7.6	5.9

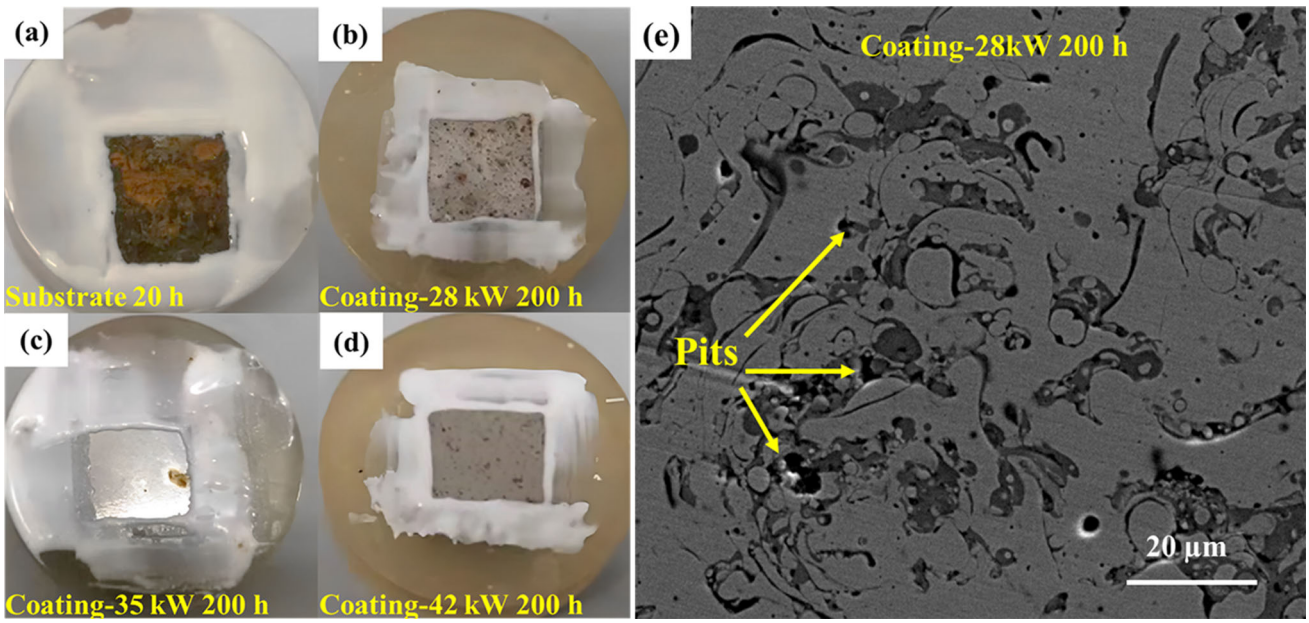

Fig. 7 Photographs of samples after salt fog test: (a) 45 steel as reference sample, Fe-based amorphous coating sprayed at different powers (b) 28 kW, (c) 35 kW and (d) 42 kW; (e) SEM image of coating-28 kW after 200 h salt spray corrosion

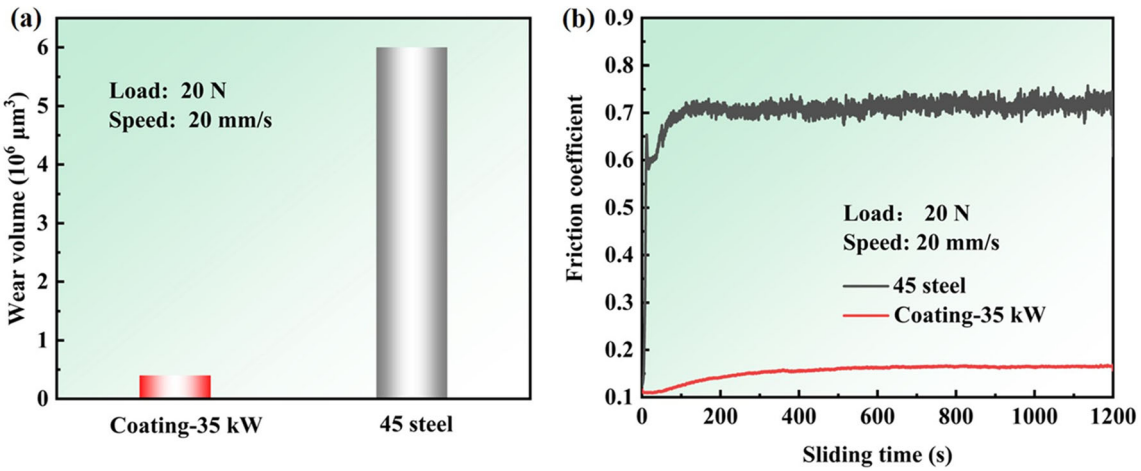

Fig. 8 Coating-35 KW and 45 steel substrate under load of 20 N and sliding speed of 20 mm/s, (a) wear volume and (b) friction coefficient curve

positioning it as a cost-effective option for protecting surfaces against friction-induced wear (Ref 21).

To understand the wear mechanism, the worn surfaces of coating-35 kW at different sliding speeds and loads were examined by SEM (Fig. 9). As shown in Fig. 9(a), almost no evidence of significant wear was observed except for a few grooves when sliding at low speed (0.02 m/s) and low load (20 N). It should be noted that the pores were formed during spraying, not during sliding. In contrast, the surface of the 45 steel produced severe wear. The surface was covered with severe furrows and peeled debris, indicating that its main wear mechanism was adhesive wear (Fig. 9b). The coating-35 kW was further tested under higher load and higher speed. As shown in Fig. 9(c), with the load increased, the width of the grooves on the surface of coating-35 kW increased significantly, but the depth of the grinding marks was not obvious, which was consistent with previous study that the wear behavior of amorphous coatings appeared to be insensitive to the applied load (Ref 41). Under the same load, increasing the sliding speed significantly enlarged the surface roughness. Under high speed (Fig. 9d), many small particles were embedded in the concave area, indicating that the coating-35 kW had abrasive wear. In addition, several micro-cracks parallel to the sliding direction appeared on the surface, which was a characteristic of fatigue wear. The wear rates under different test conditions were also calculated. Under 20 N and 20 mm/s, the wear rate of the

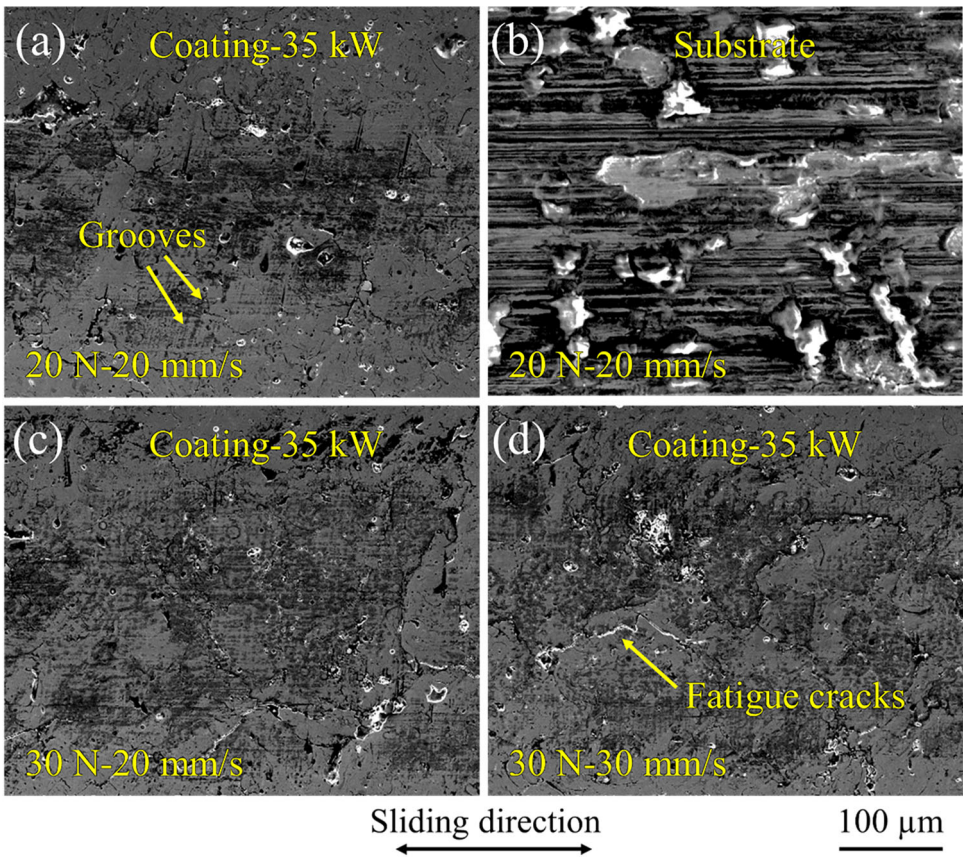

Fig. 9 SEM images of typical wear trace, (a) Coating-35 kW at 20 N and 20 mm/s, (b) Substrate at 20 N and 20 mm/s, (c) Coating-35 kW at 30 N and 20 mm/s, (d) Coating-35 kW at 30 N and 30 mm/s

coatings was about 8.3 $\times$ 10^{-7} mm^3/(N m), while at 30 N and 30 mm/s, the wear rate reached 25.9 $\times$ 10^{-7} mm^3/(N m). Delamination from fatigue wear at high speeds and high loads led to an increase in the wear rate.

The worn-off debris from coating-35 kW after being tested at 30 N and 30 mm/s was analyzed by SEM and EDS, as shown in Fig. 10(a) and (b). Here, we mainly collect the worn-off debris under the conditions of 30 N and 30 mm/s because there was limited worn-off debris under low speed and load. The size of the worn-off debris was about 2-5 μm, which mainly presented the flake-like structure with small particles (size $<$ 1 μm) attached. Four representative areas were selected for composition analysis. Oxygen elements were distributed in all four areas, which were produced from the friction heat at the contact interface. The small worn-off particle (area A) contained the highest oxygen content compared with other areas, which might be due to the rupture of the worn-off debris oxide film to participate in the new round wear test. The composition of flakes and particles of wear debris were significantly different, and the composition of the flakes was relatively close to the as-sprayed coating. The Si element in the debris came from the silicon nitride ball, indicating that the material transfer occurred during the wear process. As the wear behavior of coatings depended not only on the surface, but also on the regions beneath the surface, the cross section of the coating after wear testing was also examined. Figure 10(c) shows the SEM image of a longitudinal cross section of a wear track under the applied load of 30 N and the sliding speed of 30 mm/s. Some big cracks along the intersplat regions and small cracks perpendicular to the intersplat were observed on the cross section. Furthermore, as shown in Fig. 10(c), the height of the pits produced by material peeling was about 5 μm, which was very similar to the thickness of the fragments shown in Fig. 10(a). This finding confirmed that the substantial flake-like debris originated from the coating's detachment in areas where cracks had formed and spread. From the EDS line scan across the amorphous matrix/tribolayer (Fig. 10d), it was found that the thickness of the oxidation layer was around 3 μm and O element existed within the distance at the depth of 3 μm from the surface. The obvious enrichment indicated that the O element diffused from the surface to the interior of the coating during the friction process.

Based on the above results, it was reasonable to infer that oxidation wear was a primary wear mechanism for the amorphous coating under dry sliding conditions. The high flash temperatures generated by dry friction likely surpassed the glass transition or crystallization temperatures

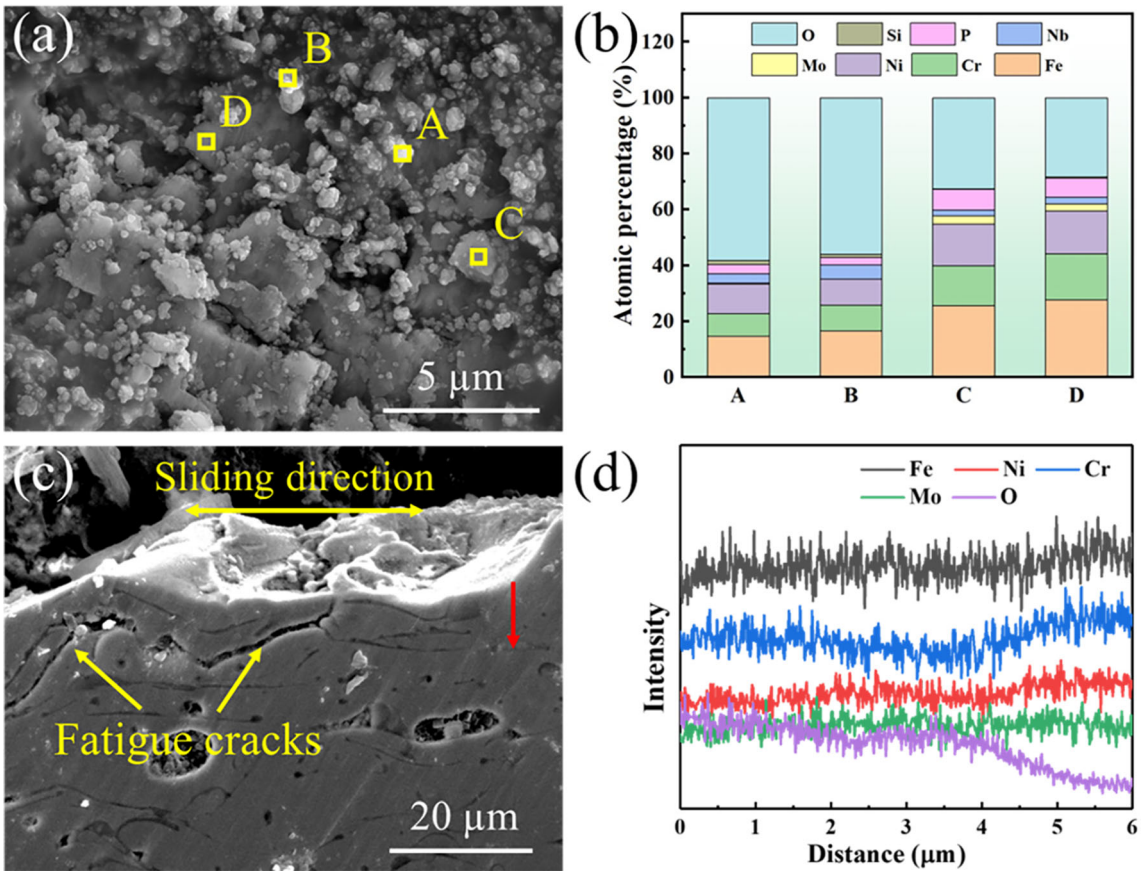

Fig. 10 (a) SEM image and (b) EDS element analysis of wear debris from coating-35 kW tested at 30 N and 30 mm/s, (c) SEM image of cross section parallel to the sliding direction of the worn coating-35 kW under an applied load of 30 N and sliding speed of 30 mm/s and (d) EDS line scan along the red arrow marked in (c)

of the coating, resulting in significant surface oxidation (Ref 21, 42). Oxygen tended to diffuse preferentially through the coating's imperfect areas, such as pores and loosely bonded intersplats, because of the heightened atomic reactivity in these zones. Typically brittle, these oxides were susceptible to peeling off once the oxide layer reached a critical thickness due to ongoing flash friction-induced heating, which in turn led to an escalated rate of wear.

Conclusions

In this work, a novel $Fe_{35}Ni_{20}Cr_{20}Mo_5Nb_xB_4C_4P_{12}Nb_1$ high-entropy amorphous alloy with enhanced GFA and good resistance was designed by the addition of 1 at.% Nb. The Fe-based high-entropy amorphous coatings with this composition were prepared by APS technology under different spray powers. The coating-35 kW exhibited the best corrosion resistance due to the combination of large amorphous content and relatively less amount of oxidation. Besides, the coating-35 kW had a high Vickers hardness of 519 ± 21 HV, low friction coefficients of 0.17, as well as a low wear rate of 8.3×10^{-7} $mm^3/$ (N m) at 20 N and 20 mm/s. The wear mechanisms of the coating-35 kW were mainly abrasive wear and oxidation wear at low speed and low load, and oxidation wear and fatigue wear at high speed and high load. The developed APS high-entropy amorphous coating has excellent corrosion resistance and wear properties, which brings a broad prospect for potential engineering applications of thermal spray high-entropy amorphous coatings.

Acknowledgments This work was supported by Jiangsu Provincial Key R&D Program (BE2021088), National Natural Science Foundation of China (52231005), Opening Project of Jiangsu Key Laboratory of Advanced Structural Materials and Application Technology (ASMA202302), Open Research Fund of Jiangsu Key Laboratory for Advanced Metallic Materials (AMM2020A01, AMM2024A02, AMM2023B05), the Start-up Research Fund of Southeast University (RF1028623113).

Authors Contribution ZG involved in conceptualization, methodology, data curation, investigation, and writing—original draft. YY involved in writing—review and editing, methodology, data curation, and investigation. ZZ involved in methodology, data curation, and investigation. BZ involved in conceptualization, methodology, and

resources. QW involved in writing—review and editing, funding acquisition, conceptualization, project administration, and supervision. BS involved in conceptualization, funding acquisition, project administration, and supervision.

Data Availability Data will be made available on request.

Competing interests The authors declare that they have no known competing financial interests or personal relationships that could have appeared to influence the work reported in this paper.

References

1. D.A. Shifler, Understanding Material Interactions in Marine Environments to Promote Extended Structural Life, *Corros. Sci.*, 2005, **47**, p 2335-2352.
2. G.H. Koch, M.P.H. Brongers, N.G. Thompson, Y.P. Virmani, and J.H. Payer, Corrosion Cost and Preventive Strategies in the United States (Final Report), 2002.
3. E. Bowman, G. Jacobson, G. Koch, J. Varney, N. Thompson, O. Moghissi, M. Gould and J. Payer, *International Measures of Prevention, Application, and Economics of Corrosion Technologies Study*, NACE International, Houston, 2016.
4. C. Jiang, W. Liu, G. Wang, Y. Chen, Y. Xing, C. Zhang and M. Dargusch, The Corrosion Behaviours of Plasma-Sprayed Fe-Based Amorphous Coatings, *Surf. Eng.*, 2018, **34**, p 634-639.
5. B. Huang, C. Zhang, G. Zhang and H. Liao, Wear and Corrosion Resistant Performance of Thermal-Sprayed Fe-Based Amorphous Coatings: A Review, *Surf. Coat. Technol.*, 2019, **377**, p 124896.
6. M.A. Faridi, S.K. Nayak, D.K.V.D. Prasad, A. Kumar and T. Laha, Effect of Microstructure and Phase Evolution on the Wear Behavior of Fe-Based Amorphous/Nanocrystalline Composite Coatings Synthesized by Plasma Spraying, *J. Therm. Spray Technol.*, 2023, **32**, p 2054-2067.
7. F. Otsubo, H. Era and K. Kishitake, Formation of Amorphous Fe-Cr-Mo-8P-2C Coatings by the High Velocity Oxy-Fuel Process, *J. Therm. Spray Technol.*, 2000, **9**, p 494-498.
8. F. Otsubo and K. Kishitake, Corrosion Resistance of Fe-16%Cr-30%Mo-(C, B, P) Amorphous Coatings Sprayed by HVOF and APS Processes, *Mater. Trans.*, 2005, **46**, p 80-83.
9. D.J. Branagan, W.D. Swank, D.C. Haggard and J.R. Fincke, Wear-Resistant Amorphous and Nanocomposite Steel Coatings, *Metall. Mater. Trans. A*, 2001, **32**, p 2615-2621.
10. H.S. Ni, X.H. Liu, X.C. Chang, W.L. Hou, W. Liu and J.Q. Wang, High Performance Amorphous Steel Coating Prepared by HVOF Thermal Spraying, *J. Alloys Compd.*, 2009, **467**, p 163-167.
11. C.W. Ziemian, W.J. Wright and D.E. Cipoletti, Influence of Impact Conditions on Feedstock Deposition Behavior of Cold-Sprayed Fe-Based Metallic Glass, *J. Therm. Spray Technol.*, 2018, **27**, p 843-856.
12. N.G. Patel, A. Kumar, V.N. Jayawardana, C.D. Woodworth and P.A. Yuya, Fabrication, Nanomechanical Characterization, and Cytocompatibility of Gold-Reinforced Chitosan Bio-nanocomposites, *Mater. Sci. Eng. C-Mater.*, 2014, **44**, p 336-344.
13. R.Q. Guo, C. Zhang, Y. Yang, Y. Peng and L. Liu, Corrosion and Wear Resistance of a Fe-Based Amorphous Coating in Underground Environment, *Intermetallics*, 2012, **30**, p 94-99.
14. Y. Wang, Y.G. Zheng, W. Ke, W.H. Sun and J.Q. Wang, Corrosion of High-Velocity Oxy-fuel (HVOF) Sprayed Iron-Based Amorphous Metallic Coatings For Marine Pump in Sodium Chloride Solutions, *Mater. Corros.*, 2012, **63**, p 685-694.
15. X.Q. Liu, Y.G. Zheng, X.C. Chang, W.L. Hou, J.Q. Wang, Z. Tang and A. Burgess, Microstructure and Properties of Fe-Based Amorphous Metallic Coating Produced by High Velocity Axial Plasma Spraying, *J. Alloys Compd.*, 2009, **484**, p 300-307.
16. D. Zois, A. Lekatou and M. Vardavoulias, Preparation and Characterization of Highly Amorphous HVOF Stainless Steel Coatings, *J. Alloys Compd.*, 2010, **504**, p S283-S287.
17. R.Q. Guo, C. Zhang, Q. Chen, Y. Yang, N. Li and L. Liu, Study of Structure and Corrosion Resistance of Fe-Based Amorphous Coatings Prepared by HVAF and HVOF, *Corros. Sci.*, 2011, **53**, p 2351-2356.
18. J.C. Farmer, D. Day, T. Lian, C.-K. Saw, P. Hailey, J. Payer, L. Aprigliano, B. Beardsley and D. Branagan, *Long-Term Corrosion Testing of Thermal Spray Coatings of Amorphous Metals:* $Fe_{49.7}Cr_{17.7}Mn_{1.9}Mo_{7.4}W_{1.6}B_{15.2}C_{3.8}S_{i2.4}$ *and* $Fe_{48}Mo_{14}Cr_{15}Y_{2}C_{15}B_{6}$. *UCRL-CONF-232604*, Lawrence Livermore National Laboratory, Livermore, 2007.
19. J.C. Farmer, J.-S. Choi, C.-K. Saw, R.H. Rebak, S.D. Day, T. Lian, P.D. Hailey, J.H. Payer, D.J. Branagan and L.F. Aprigliano, *Long-Term Corrosion Tests of Prototypical SAM2X5* ($Fe_{49.7}Cr_{17.7}Mn_{1.9}Mo_{7.4}W_{1.6}B_{15.2}C_{3.8}S_{i2.4}$) *Coating. UCRL-TR-230923*, Lawrence Livermore National Laboratory, Livermore, 2007.
20. H.R. Ma, J.W. Li, C.T. Chang, X.M. Wang and R.W. Li, Passivation Behavior of Fe-Based Amorphous Coatings Prepared by High-Velocity Air/Oxygen Fuel Processes, *J. Therm. Spray Technol.*, 2017, **26**, p 2040-2047.
21. H.R. Ma, X.Y. Chen, J.W. Li, C.T. Chang, G. Wang, H. Li, X.M. Wang and R.W. Li, Fe-Based Amorphous Coating with High Corrosion and Wear Resistance, *Surf. Eng.*, 2017, **33**, p 56-62.
22. Y.Y. Ge, J.B. Cheng, J.Y. Mo, L. Xue, B.S. Zhang, S. Hong, Y.P. Wu, X.B. Liang and X.C. Zhang, Experimental and DFT Studies on Corrosion Behaviors of Laser-Cladded $(FeCoNi)_{75-x}Cr_xB_{15}Si_{10}$ High-Entropy Alloy Coatings, *J. Alloys Compd.*, 2024, **976**, p 173173.
23. Y. Li, S. Wang, X. Wang, M. Yin and W. Zhang, New FeNiCrMo(P, C, B) High-Entropy Bulk Metallic Glasses with Unusual Thermal Stability and Corrosion Resistance, *J. Mater. Sci. Technol.*, 2020, **43**, p 32-39.
24. F. Shu, B. Zhang, T. Liu, S. Sui, Y. Liu, P. He, B. Liu and B. Xu, Effects of Laser Power on Microstructure and Properties of Laser Cladded CoCrBFeNiSi High-Entropy Alloy Amorphous Coatings, *Surf. Coat. Technol.*, 2019, **358**, p 667-675.
25. J.B. Cheng, B. Sun, Y.Y. Ge, X.L. Hu, L.H. Zhang, X.B. Liang and X.C. Zhang, Effect of B/Si Ratio on Structure and Properties of High-Entropy Glassy Fe25Co25Ni25(BxSi1-x)25 Coating Prepared by Laser Cladding, *Surf. Coat. Technol.*, 2020, **402**, p 126320.
26. F. Zhai, E. Pineda, M.J. Duarte and D. Crespo, Role of Nb in Glass Formation of Fe-Cr-Mo-C-B-Nb BMGs, *J. Alloys Compd.*, 2014, **604**, p 157-163.
27. D. Janovszky, M. Sveda, A. Sycheva, F. Kristaly, F. Zamborszky, T. Koziel, P. Bala, G. Czel and G. Kaptay, Amorphous Alloys and Differential Scanning Calorimetry (DSC), *J. Therm. Anal. Calorim.*, 2022, **147**, p 7141-7157.
28. H.J. Sun, Q.K. Man, Y.Q. Dong, B.L. Shen, H. Kimura, A. Makino and A. Inoue, Effect of Nb Addition on the Glass-Forming Ability, Mechanical and Soft-Magnetic Properties in $(Co_{0.942}Fe_{0.058})_{72-x}Nb_xB_{22.4}Si_{5.6}$ Bulk Glassy Alloys, *J. Alloys Compd.*, 2010, **504S**, p S31-S33.
29. J.H. Yao, H. Yang, J. Zhang, J.Q. Wang and Y. Li, The Influence of Nb and Zr on Glass-Formation Ability in the Ternary Fe-Nb-B and Fe-Zr-B and Quaternary Fe-(Nb, Zr)-B Alloy Systems, *J. Mater. Res.*, 2008, **23**, p 392-401.

30. W.J. Botta, J.E. Berger, C.S. Kiminami, V. Roche, R.P. Nogueira and C. Bolfarini, Corrosion Resistance of Fe-Based Amorphous Alloys, *J. Alloys Compd.*, 2014, **586**, p S105-S110.
31. M.C. Gao, J.W. Yeh, P.K. Liaw and Y. Zhang, *High-Entropy Alloys: Fundamentals and Applications*, Springer, Cham, 2016, p 5-12
32. S.J. Pang, T. Zhang, K. Asami and A. Inoue, New Fe-Cr-Mo-(Nb, Ta)-C-B Glassy Alloys with High Glass-Forming Ability and Good Corrosion Resistance, *Mater. Trans. Jim*, 2001, **42**, p 376-379.
33. C.A.C. Souza, J.E. May, I.A. Carlos, M.F. de Oliveira, S.E. Kuri and C.S. Kiminami, Influence of the Corrosion on the Saturation Magnetic Density of Amorphous and Nanocrystalline $Fe_{73}Nb_{3}Si_{15.5}B_{7.5}Cu_{1}$ and $Fe_{80}Zr_{3.5}Nb_{3.5}B_{12}Cu_{1}$ Alloys, *J. Non Cryst. Solids*, 2002, **304**, p 210-216.
34. E.S. Barreto, M. Frey, J. Wegner, A. Jose, N. Neuber, R. Busch, S. Kleszczynski, L. Mädler and V. Uhlenwinkel, Properties of Gas-Atomized Cu-Ti-Based Metallic Glass Powders for Additive Manufacturing, *Mater. Des.*, 2022, **215**, p 110519.
35. P. Wesseling, B.C. Kok and J.J. Lewandowski, Quantitative Evaluation of a-Al Nano-particles in Amorphous $Al_{87}Ni_{7}Gd_{6}$—Comparison of XRD, DSC, and TEM, *Scr. Mater.*, 2003, **48**, p 1537-1541.
36. S.K. Nayak, A. Kumar, K. Sarkar, A. Banerjee and T. Laha, Mechanistic Insight into the Role of Amorphicity and Porosity on Determining the Corrosion Mitigation Behavior of Fe-Based Amorphous/Nanocrystalline Coating, *J. Alloys Compd.*, 2009, **849**, p 156624.
37. Y.Z. Ye, Z.J. Guo, Z.J. Zhou, B.S. Zhang, Q.Q. Wang and B.L. Shen, Improved Corrosion and Corrosion-Wear Properties of Fe-Based High-Entropy Amorphous Coatings by Modulating Heat Input of HVAF, *Corros. Sci.*, 2024, **232**, p 112049.
38. C. Zhang, R.Q. Guo, Y. Yang, Y. Wu and L. Liu, Influence of the Size of Spraying Powders on the Microstructure and Corrosion Resistance of Fe-Based Amorphous Coating, *Electrochim. Acta*, 2011, **56**, p 6380-6388.
39. A. Kumar, R. Kumar, P. Bijalwan, M. Dutta, A. Banerjee and T. Laha, Fe-Based Amorphous/Nanocrystalline Composite Coating by Plasma Spraying: Effect of Heat Input on Morphology, Phase Evolution and Mechanical Properties, *J. Alloys Compd.*, 2019, **771**, p 827-837.
40. A. Kumar, S.K. Nayak, K. Sarkar, A. Banerjee, K. Mondal and T. Laha, Investigation of Nano- and Micro-scale Structural Evolution and Resulting Corrosion Resistance in Plasma Sprayed Fe-Based (Fe-Cr-B-C-P) Amorphous Coatings, *Surf. Coat. Technol.*, 2020, **397**, p 126058.
41. C. Zhang, L. Liu, K.C. Chan, Q. Chen and C.Y. Tang, Wear Behavior of HVOF-Sprayed Fe-Based Amorphous Coatings, *Intermetallics*, 2012, **29**, p 80-85.
42. J. Kong, D. Xiong, J. Li, Q. Yuan and R. Tyagi, Effect of Flash Temperature on Tribological Properties of Bulk Metallic Glasses, *Tribol. Lett.*, 2009, **35**, p 151-158.